CrossMark

Hybrid photonic–plasmonic crystal nanocavity sensors

Pi-Ju Cheng[1] · Chih-Kai Chiang[2] · Bo-Tsun Chou[3] · Zhen-Ting Huang[4] · Yun-Cheng Ku[5] · Mao-Kuen Kuo[5] · Jin-Chen Hsu[6] · Tzy-Rong Lin[2,4]

Abstract

We have investigated a hybrid photonic–plasmonic crystal nanocavity consisting of a silicon grating nanowire adjacent to a metal surface with a gain gap between them. The hybrid plasmonic cavity modes are highly confined in the gap due to the strong coupling of the photonic crystal cavity modes and the surface plasmonic gap modes. Using finite-element method (FEM), guided modes of the hybrid plasmonic waveguide (WG) were numerically determined at a wavelength of 1550 nm. The modal characteristics such as WG confinement factors and modal losses of the fundamental hybrid plasmonic modes were obtained as a function of groove depth at various gap heights. Furthermore, the band structure of the hybrid crystal modes corresponding to a wide band gap of 17.8 THz is revealed. To enclose the optical energy effectively, a single defect was introduced into the hybrid crystal. At a deep subwavelength defect length as small as 270 nm, the resonant mode exhibits a high quality factor of 567 and an ultrasmall mode volume of 1.9×10^{-3} $(\lambda/n_{\text{eff}})^3$ at the resonance wavelength of 1550 nm. Compared to conventional photonic crystal nanowire cavities in the absence of a metal surface, the factor Q/V_{m} is significantly enhanced by about 15 times. The designed hybrid photonic–plasmonic cavity sensors exhibit distinguished characteristics such as sensitivity of 443 nm/RIU and figure of merit of 129. The proposed nanocavities open new possibilities for various applications with strong light–matter interaction, such as biosensors and nanolasers.

1 Introduction

Various nanocavities with high quality factor (Q) and small mode volume (V_{m}) have attracted considerable interest due to their potential in strong light–matter interactions [1]. Conventional photonic microcavities, such as microspheres [2], microtoroid [3] and photonic crystal (PhC) cavities [4], have demonstrated the capability of confining the modal field efficiently. They also exhibited extremely high Q factors of over 10^5–10^6. However, the footprint of optical modes associated with these cavities is still limited by the diffraction limit. On the other hand, plasmonic cavities supporting surface plasmon polaritons (SPPs) reduce the effective mode volumes of these composite excitations of photons, and charge oscillations well below the diffraction limit [5–11]. With the advancement of SPP-based technologies, various plasmonic nanocavities [12–19], especially those that possess the plasmonic gap resonances, have recently been investigated [20–23]. Nevertheless, Q factors for this type of cavities are usually limited by the parasitic loss of metal surroundings. To achieve a high Q/V_{m} ratio, which is an important parameter characterizing the light–matter interactions in nanocavities, Yang et al. [24] have demonstrated photonic-plasmonic crystal (PhPC) nanocavities by integrating the one-dimensional (1D) PhC structure into plasmonic waveguides (WGs). This approach not only successfully produced a coherent light spot deep in the subwavelength scale, but also achieved sufficiently high Q factors.

✉ Tzy-Rong Lin
  trlin@ntou.edu.tw

  Jin-Chen Hsu
  hsujc@yuntech.edu.tw

[1] Research Center for Applied Sciences, Academia Sinica, Taipei 11529, Taiwan

[2] Institute of Optoelectronic Sciences, National Taiwan Ocean University, Keelung 20224, Taiwan

[3] ATD Device, United Microelectronics Corporation, Hsinchu 30075, Taiwan

[4] Department of Mechanical and Mechatronic Engineering, National Taiwan Ocean University, Keelung 20224, Taiwan

[5] Institute of Applied Mechanics, National Taiwan University, Taipei 10617, Taiwan

[6] Department of Mechanical Engineering, National Yunlin University of Science and Technology, Yunlin 64002, Taiwan

In this paper we analyze a hybrid PhPC nanocavity containing a silicon (Si) nanowire (NWR) PhC near the metal surface. With a periodic dielectric lattice on the top of the metal layer, hybrid PhPC can be formed to support the complete one-dimensional (1D) bandgap [25] of the hybrid plasmonic structure. A defect structure is further introduced into the PhC NWR to confine the optical energy. First, modal characteristics of the hybrid plasmonic guided modes are investigated at various gap heights and indentation depths using FEM [21]. The dispersion relation of this hybrid PhPC structure is provided as well. As the photonic defect is introduced into the corrugated NWR, a resonant mode is formed and tightly confined inside the region of the air gaps. Its Q factor can be as high as 567, and an ultrasmall mode volume of 1.9×10^{-3} $(\lambda/n_{eff})^3$ can be achieved, where λ and n_{eff} are the wavelength and effective index of the mode, respectively. The proposed nanocavity has a high Q/V_m ratio of approximately 3.0×10^5 $(\lambda/n_{eff})^{-3}$ and can also enhance the light–matter interaction, which is of significant importance in various kinds of applications such as cavity quantum electrodynamics (QED), nonlinear optics, low-threshold nanoscale lasers, optomechanics, surface-enhanced Raman scattering (SERS) [26, 27], and biological sensors [28, 29].

The proposed NWR platform is a bottom-up approach and may have the potential for label-free and lab-on-chip biosensing. The small cavity defined by the photonic defect in this 1D PhC on a Si NWR can be milled by a focused ion beam [30] or chemical wet etching on selective modulation-doped regions of the Si NWR [31]. Resonant modes with a high Q/V_m ratio are quite sensitive to variation of the refractive index n_c of surrounding media. The extremely small volume V_m of the cavity mode automatically determines a compact sensing area with a sufficiently large sensitivity. Meanwhile, the nanocavity immersed into liquid analytes can act as an optical sensor, which responds to variations of the index due to real-time reactions of biomolecules/proteins in aqueous solutions or density changes of glucose in fluids [32, 33]. The Q factor corresponding to the conceptual scheme described above at $n_c = 1.33$ (water) was also calculated, and the sensitivities at other values of n_c were determined as well. In addition, the effects of metal were studied by comparing modal characteristics of the hybrid plasmonic nanocavity to those of a NWR PhC defect cavity, below which the metal layer is replaced by the dielectric (grooved nanorod placed on top of a complete dielectric substrate). It is known that there are trade-offs between sensitivities (S) and Q factors in label-free sensors based on optical resonators. A higher Q factor usually implies a modal distribution that spreads less into the ambient environment; hence, the detection is less efficient. In this study, the theoretically demonstrated PhPC nanocavity has a relatively high sensitivity of 443 and a large Q factor of 450 in aqueous solutions. This structure can be used as label-free biosensor in lab-on-a-chip devices based on a bottom-up technology [32].

2 Characteristics of guided modes

The proposed hybrid plasmonic nanocavity is illustrated in Fig. 1. The structure consists of a patterned Si NWR and a silicon-dioxide (SiO_2) gap layer on a flat silver (Ag) substrate. The patterned NWR is a 1D PhC in the ambient environment ($n_c = 1$). The NWR-SiO_2-Ag structure supports hybrid modes whose optical field intensity is strongly confined within the gap layer that has the lowest refractive index among the three materials. The hybrid plasmonic gap modes are coupled to Bloch modes of the dielectric NWR PhC to form hybrid PhPC modes. Parameters of the proposed structure such as the NWR groove depth d, the gap height h, and period Λ shown in Fig. 1 are varied to optimize the design for high Q factor and low mode volume. Beside these parameters, radius R of the unprocessed Si NWR is fixed at 150 nm.

First, to achieve a high Bragg reflection, the methods to obtain a high contrast of effective indices along the NWR PhC at a wavelength λ of 1550 nm were investigated. The groove depth d was varied to achieve suitable effective indices n_{eff}. As shown in Fig. 2, the real parts Re(n_{eff}) of the effective index, propagation lengths $(2k_0\text{Im}(n_{eff}))^{-1}$, WG confinement factors (overlap with the gap region of SiO_2), and mode areas were obtained as a function of d under different gap heights h. As the groove depth d reduces to zero, the overall configuration approaches the bare NWR with a radius of $R = 150$ nm placed on the SiO_2/Ag substrate. The hybrid plasmonic structure on the dielectric/metal substrate can be regarded as effective high–low-index bilayers arranged sequentially along the NWR-axis. It exhibits an extremely small footprint confined in the low-index region of SiO_2 gap. The real part of the effective index of the plasmonic gap mode has a maximum at Re(n_{eff}) = 2.2 and the maximum WG confinement factor is about 0.4 at $d = 0$ and $h = 20$ nm. As the groove depth d increases, the air gap becomes wider, and a larger part of the field can occupy the region of air underneath the NWR, in which the refractive index is unity. Therefore, the degree of confinement inside the dielectric layer of SiO_2 drops. The coupling strength of the fundamental hybrid plasmonic gap mode is also affected by the gap height h of the SiO_2 layer. For the lower height h, the poorer confinement in the gap region underneath the NWR leads to a lower confinement factor and a smaller mode area.

At a groove depth d larger than 40 nm, the characteristics of the fundamental hybrid mode starts to change significantly, as can be seen from the propagation distances in Fig. 2b. Under such conditions, the true radius of the Si

Fig. 1 a Top (oblique) view, **b** front view (*xy* plane), and **c** side view (*yz* plane) of the proposed nanocavity. The Si NWR with periodic dielectric lattice is placed on the top of the substrate and separated from the Ag bulk by a SiO$_2$ gap layer
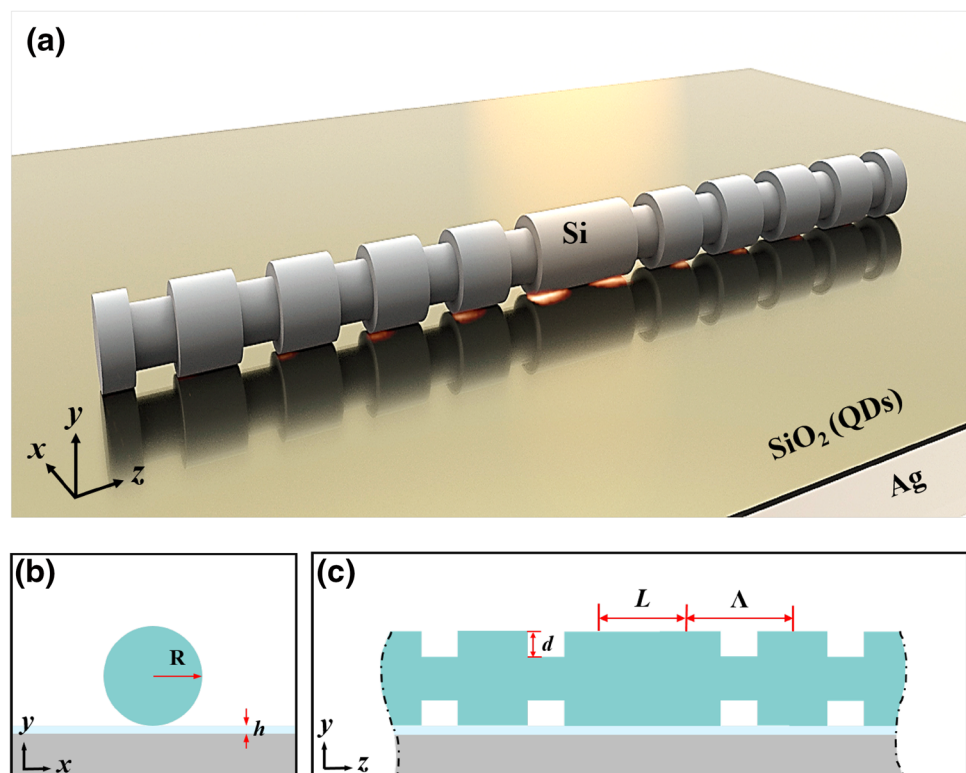
NWR, $R - d$, is sufficiently small so that the photonic mode of the bare Si NWR is no longer confined well in the Si core. As a result of the poor confinement, this mode significantly spreads into the ambient environment ($n_c = 1$), and the prominent field component outside the Si core starts to be converted into a surface-like mode of the SiO$_2$/Ag substrate. Thus, the propagation distances fall quickly with d when it becomes larger than 40 nm, reflecting the larger part of the field near the metal. Nevertheless, at a moderate d, the propagation distance can be as long as 100 μm. Therefore, for a better confinement and lower modal loss of the fundamental hybrid plasmonic mode, d was chosen as 40 nm and the gap height h was set to a moderate value of 10 nm. The real part of the corresponding effective index Re(n_{eff}) was 1.15, which was much smaller than that of the bare NWR (Re(n_{eff}) = 2.1) at $d = 0$. This high index contrast ensures the formation of a large bandgap for TM-like modes, as the PhC structure was introduced into the hybrid plasmonic WG composed of the Si NWR and the SiO$_2$/Ag substrate.

3 Cavity design

Figure 1c shows structural parameters of defect nanocaity and the unit cells of the PhC, on which periodical grooves were created along the NWR-axis (*z*-axis). The period Λ of the unit cells is 450 nm, and the width of each groove is 270 nm, both of which were previously determined by the

Bragg condition for plane waves propagating along the *z* direction [34]. The filling factor was chosen to maximize the bandgap of the TM-like modes and shift the center of the gap to the target wavelength of 1550 nm. Figure 3 shows the band structure of the hybrid PhC for both the TM-like and TE-like modes. A bandgap is clearly visible from 179.8 to 207.6 THz between the fundamental and the first-order TM-like modes, while other higher-order modes below the light cone (the region above the light blue line) are also present. Figure 4 shows the corresponding field distributions (|**E**|) of the four lowest band-edge modes at the Brillouin zone boundary. The lowest two modes are TM-like hybrid plasmonic Bloch modes with a major field component E_y. The two higher modes are TE-like with a major field component E_x. In contrast to the TE-like modes illustrated in Fig. 4c, d, the TM-like counterparts at the band-edge are strongly concentrated in the low-index gap region of the SiO$_2$, underneath the Si NWR, as shown in Fig. 4a, b.

Based on the dispersion relations of the hybrid PhC shown in Fig. 3, a defect cavity was designed to support resonant modes, which were tightly squeezed into the gap region. To examine the confinement of optical energy in the nanocavity, the number of periods at each side of the defect region was varied to understand the relationship between the corresponding reflectivity and the size of the PhC segments. Three-dimensional (3D) FEM and the orthogonality theorem of WG modes were used in these calculations [4]. The result shows that the reflectivity is proportional to

(a)

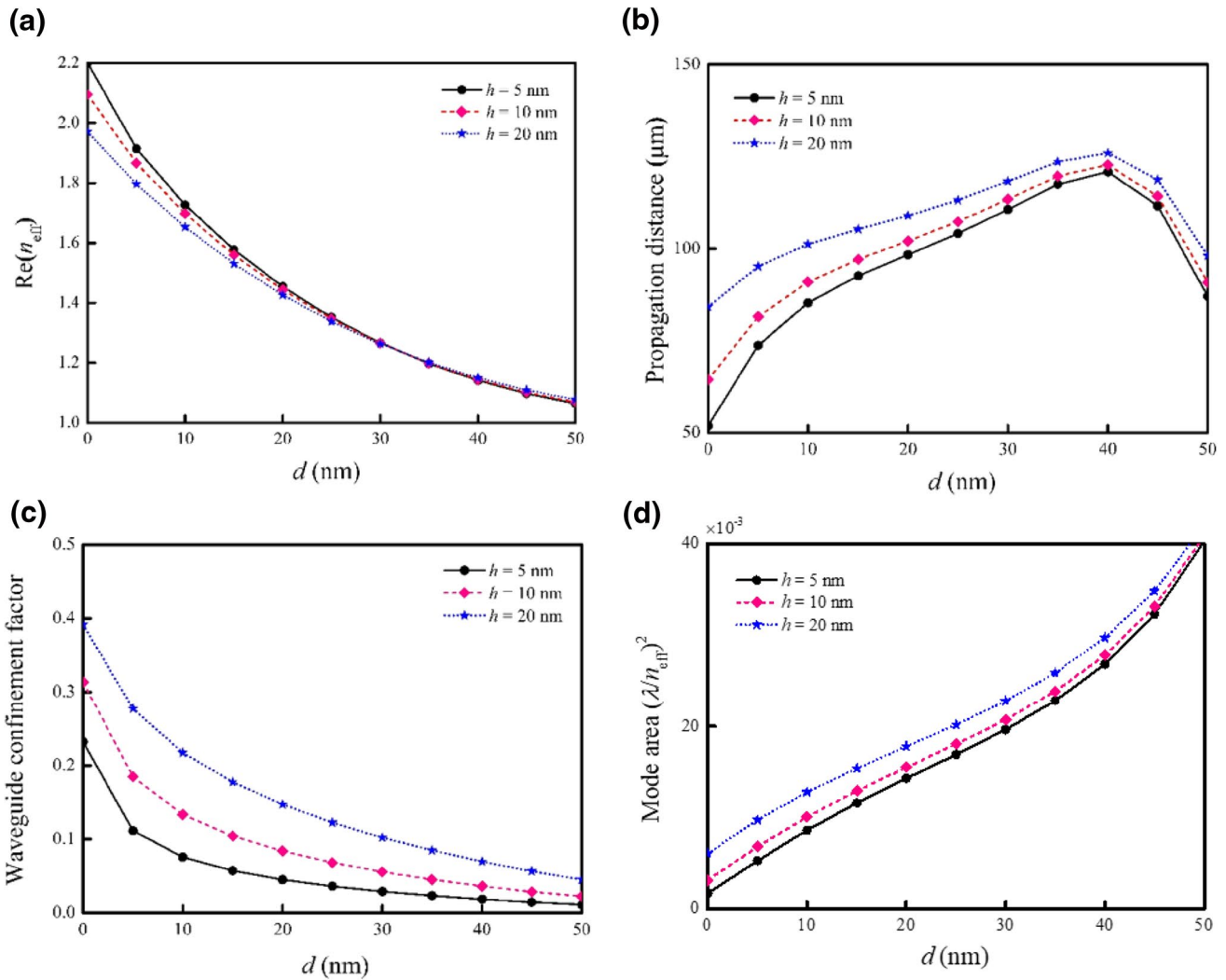**(b)**

(c)

(d)

Fig. 2 **a** Real parts of the effective index, **b** propagation distances, **c** WG confinement factors, and **d** mode areas of the fundamental plasmonic hybrid gap mode as a function of the groove depth d at $R=150$ nm and $h=5$, 10, and 20 nm, respectively
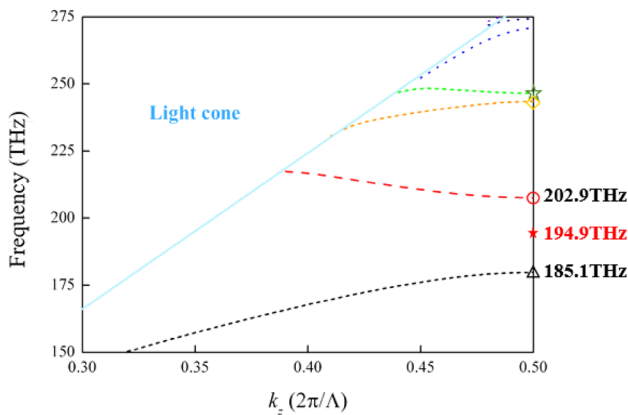

Fig. 3 Dispersion relations of the hybrid PhPC. The two lower bands correspond to the TM-like bands, and the higher two bands correspond to the TE-like bands. The light cone is indicated by the region above the light blue line

the number of periods at the beginning, and then gradually converges to a constant magnitude. Sufficiently small losses were obtained when the PhC segment was composed of eight periods of bare/corrugated NWR pairs. For the hybrid plasmonic nanocavity, the Q factor of the resonant mode was determined at a defect length $L=270$ nm using 3D FEM calculations. Furthermore, field profiles of the high-Q cavity mode with a resonance wavelength λ_p of 1550 nm were studied, at which the coherent light source is commercially available as semiconductor lasers for telecommunication.

The field profiles of the resonant mode viewed from different angles are shown in Fig. 5a–c. In Fig. 5b, the side view (yz plane) of the field profile reveals a strong localization in the gap and air regions below the Si NWR, whereas the top-view (xz plane) at the middle of the gap layer indicates that the field decays toward the PhPC segment at each side of the defect region. The field profile of the eigenmode

Fig. 4 Field distributions (|**E**|) of the **a** first, **b** second, **c** third, and **d** fourth band-edge modes at the Brillouin zone boundary, as indicated in Fig. 3. Modes in (**a**) and (**b**) are TM-like, while the counterparts in (**c**) and (**d**) are TE-like
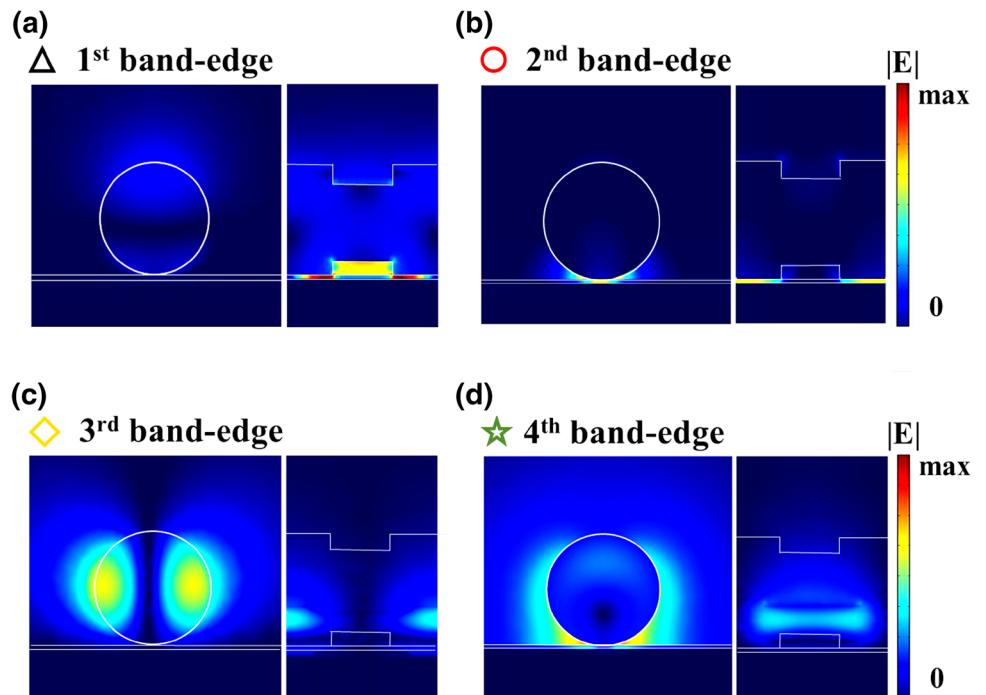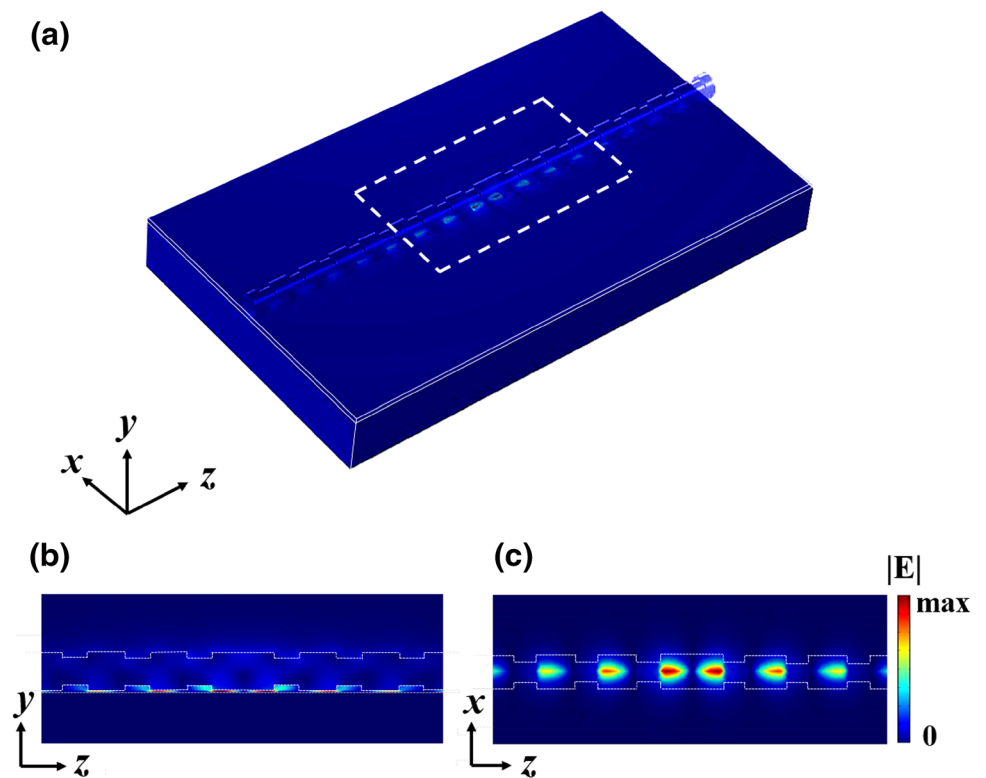

Fig. 5 **a** Oblique view, **b** side view (*yz* plane), and **c** top-view (*xz* plane, at the middle of the gap layer) of the mode profiles corresponding to a defect length *L* of 270 nm

is evenly distributed along the *z*-axis. The *Q* factor of this mode was also calculated. In the 3D FEM calculations, we excite the nanocavity with a $\hat{y}$-polarized plane wave whose wavelength is swept across the resonance of the mode. The square magnitude of the electric field (proportional to the electric energy density) inside the gap region was spatially integrated and recorded at each wavelength. The corresponding spectral dependence is shown in Fig. 6. The *Q* factor was calculated as the ratio between the full width at half maximum (FWHM) and the peak wavelength λ_p of the resonance
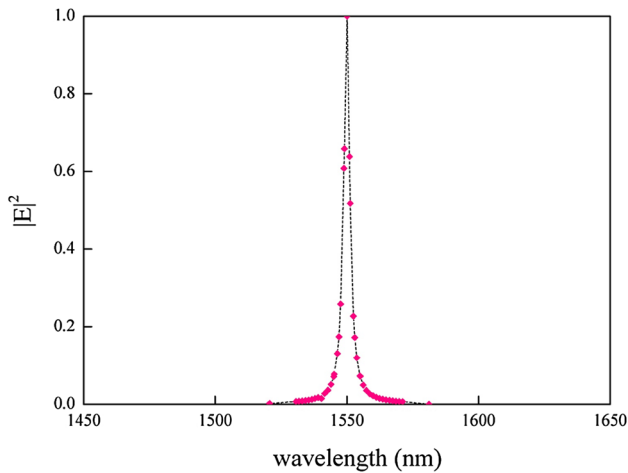
Fig. 6 Resonance line shape obtained from 3D FEM calculations for the mode at a defect length $L = 270$ nm and gap height $h = 10$ nm. The corresponding FWHM is 2.7 nm and the Q factor is 567
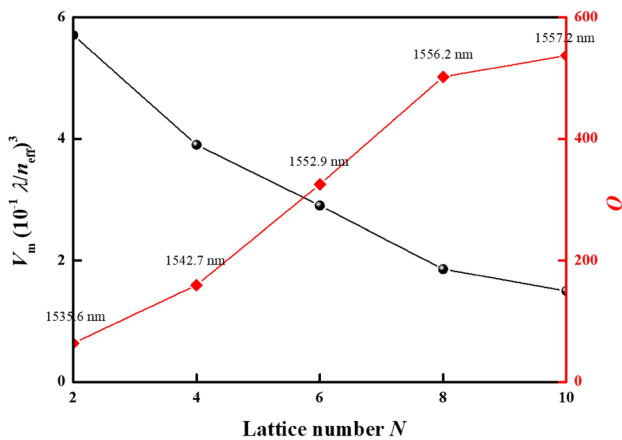

Fig. 7 Q factor and the effective mode volume V_m versus the number N of PhC unit cells at each side of the NWR defect cavity

lineshape. By resolving the field distribution of the resonance modes, the mode volume V_m can be obtained [15]. As can be seen in Fig. 6, with a FWHM of about 2.7 nm and a resonance wavelength λ_p of 1550 nm, the Q factor of this resonant mode in the defect cavity is 567. The mode volume V_m can also be determined from the field profile in Fig. 5 as 1.9×10^{-3} $(\lambda/n_{eff})^3$.

To understand the dependence of the loss at resonance of the nanocavity on the number N of the PhC unit cells at each side of the NWR, the Q factor at different N numbers was also investigated, as shown in Fig. 7. Considering the two types of losses present in the plasmonic cavity, the absorption loss is due to the metal and the radiation loss is due to photon leakage. The former is almost unaffected by the reflectivity of PhPC segments (used as end mirrors), while the latter depends on both the reflectivity and transmissivity of these hybrid photonic-plasmonic structures. The PhPC at each side of the cavity restrains the power leakage from the end facets of the Si NWR. Increasing the number N of the unit cells is an efficient way to reduce the power output from the end facets. The resonance peak is slightly red-shifted from the target wavelength of 1550 nm as the number N of the unit cells increases. The shifted resonance wavelengths are also marked on the data points in Fig. 7. The dependence of the mode volume V_m on N is also shown in Fig. 7 for comparison. At larger N values, optical fields of the cavity mode are better confined inside the defect region, but beneath the Si NWR (the gap region of SiO_2), and thereby, the corresponding effective volume of the mode decreases.

4 Toward biosensing

A unique characteristic of plasmonic hybrid gap modes is the high sensitivity to local changes of the refractive indices of ambient materials. This feature is a result of the surface field that significantly penetrates into the surrounding regions. Once the defect region introduced into the PhC NWR is placed on the substrate, the tail of the surface field can be coupled to the defect mode, and the modal fields can be squeezed into the extremely small defect region. In this manner, a hybrid cavity is formed, and the cavity mode inherently exhibits a strong response to index changes of the surroundings of the defect region. This property makes the hybrid nanocavity capable of detecting local variations of refractive indices, and making it promising for applications in chemical detection and biosensing.

Sensitivity S is the shift of the resonance wavelength λ_p per unit change of the refractive index n_c at the position of measurements, defined as $S \equiv \partial\lambda_p/\partial n_c$. The common unit adopted for sensitivity S is nm/RIU, where RIU stands for refractive index unit. A high S sensitivity is essentially required for the better performance of an index sensor. Therefore, in Fig. 8, the wavelength shifts of the cavity resonance were obtained from the resonance spectra (each spectrum is similar to that in Fig. 6, but with a shifted peak wavelength) over a broad range of refractive indices n_c. The variation of n_c, may be due to the substitution of different aqueous solutions. From $n_c = 1.0$–1.4, sensitivity S is about 440 nm/RIU. However, the increase of the environmental index inevitably deteriorates the field confinement inside the cavity because the index contrast between the environment and SiO_2 gap ($n \approx 1.5$) may not be sufficiently large to sustain the plasmonic gap modes. The smaller index contrast does not cause the drop of sensitivities, but it definitely leads to a relatively lower Q factor.

In addition, the linewidth of the resonance has to be taken into account during the design of resonance structures. The
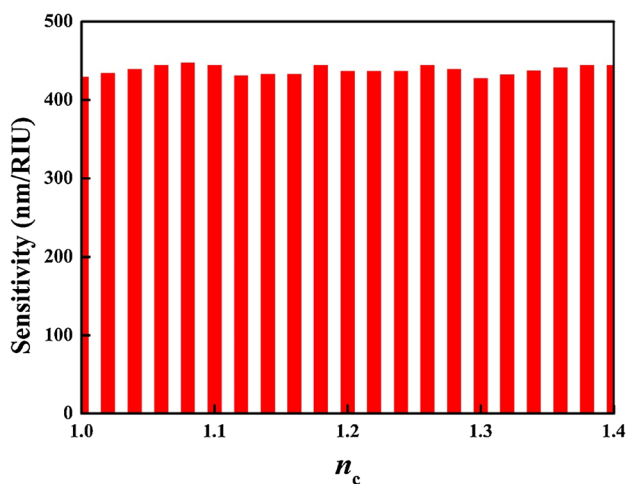
Fig. 8 Sensitivity as a function of environmental refractive indexes n_c

linewidth limits the spectral resolution of resonance-based index sensors. Therefore, a narrower linewidth is necessary for measuring a small change in the index. The Q factor is inversely proportional to the linewidth. The nanocavity investigated in this study indeed exhibits a sufficiently high Q factor of more than 550 in an open environment. In an aqueous solution with $n_c = 1.33$, an alternative design of hybrid nanocavities may be adopted with a sufficiently high Q factor of 440 at $d = 180$ nm, $\Lambda = 775$ nm, and $h = 10$ nm. The structural parameters were determined according to the procedures discussed in the previous sections. Number N of the unit cells on each side of the NWR was set to 12, which is larger compared to that ($N = 8$) in an open environment ($n_c = 1$) to keep the Q factor above 400. A large Q factor of 450 and a high sensitivity S of 443 nm/RIU can be achieved in this case. It is customary to define a figure of merit (FOM) to evaluate the performance of these resonance-based sensors. Conventionally, this factor of evaluation is expressed as $\mathrm{FOM} \equiv S/\mathrm{FWHM} = SQ/\lambda_p$. For the nanocavities proposed in this study, the FOM is about 129, which is relatively high compared to those of other sensing schemes.

Finally, a comparison is shown between a NWR PhC nanocavity, which is simply placed on a SiO_2 substrate and our proposed hybrid PhPC nanocavity. Both structures exhibit a photonic defect. The resonant mode in the former structure is denoted as "photonic mode," and the counterpart in the latter is denoted as "hybrid mode." The mode profiles

of the two types of resonant modes are shown in Fig. 9a, b. It can be seen in Fig. 9a that without the metallic substrate, the dominant field component of the photonic mode in the NWR PhC defect cavity is an even function with respect to the center of the defect region, and exhibits an antinode there. This mode is well confined inside the NWR and shows a high sensitivity to the environmental changes ($S \approx 142$ nm/ RIU). However, the hybrid mode (plasmonic gap mode) exhibits an even stronger confinement inside the low-index gap of SiO_2. Interestingly, the dominant field component of the hybrid mode is asymmetric, as can be seen from the node at the center of the defect region shown in Fig. 9b. Nevertheless, the hybrid mode exhibits a large Q factor and a small effective mode volume. The corresponding FOM is, therefore, much higher than that of the photonic mode in the NWR PhC nanocavity, which has no coupling to surface-like waves of the metallic structures. The characteristics of these two types of modes are listed in Table 1 for comparison. Despite the parasitic metal loss, the hybrid plasmonic defect resonance exhibits a relatively high sensitivity of 443 and a large Q factor of 450 in aqueous solutions ($n_c = 1.33$).

5 Conclusions

We have proposed a hybrid PhPC nanocavity, which contains a Si NWR placed on an Ag substrate with a thin SiO_2 gap layer. The modal characteristics of the hybrid plasmonic WG modes were analyzed at various gap heights and groove depths using FEM calculations. The dispersion relations of the Bloch modes in this hybrid PhPC were also solved numerically. As a defect region was introduced into the PhC, a resonant mode was formed and strongly confined inside the gap region. For these cavities, a high Q

Table 1 Comparison of the two types of resonant modes shown in Fig. 9

	Photonic mode	Hybrid mode
Q	124	450
V_m $(\lambda/n_{eff})^3$	3.6×10^{-2}	1.0×10^{-3}
Q/V_m $(\lambda/n_{eff})^{-3}$	3.4×10^3	4.4×10^5
S (nm/RIU)	142	443
FOM	17	129

Fig. 9 **a** Field distributions of the resonant mode in a PhC nanocavity made of Si NWR, which is simply placed on a SiO_2 substrate (photonic mode). **b** Counterpart of the hybrid PhPC nanocavity (hybrid mode)
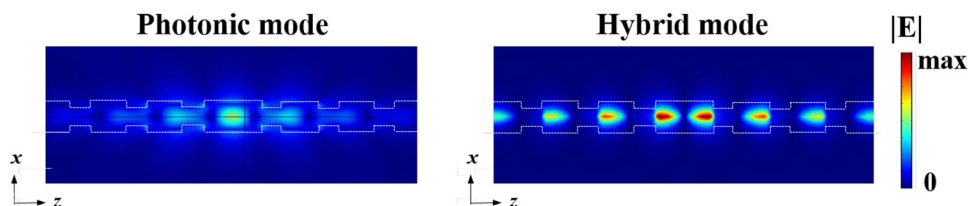
factor of about 567 and an ultrasmall mode volume smaller than 1.9×10^{-3} $(\lambda/n_{\text{eff}})^3$ can be achieved. Immersion of the proposed nanocavities in water ($n_c = 1.33$) or other aqueous solutions were examined to evaluate the sensitivity and FOM for biosensing. The results demonstrate that the defect mode of the hybrid PhPC structure made of NWRs can reach a sensitivity of 443 nm/RIU, an FWHM of 3.4 nm, and an FOM of 129 at the wavelength of about 1550 nm.

References

1. Y. Yamamoto, R.E. Slusher, Optical processes in microcavities, (Springer, Boston, MA, 1995) pp. 871–878
2. K.J. Vahala, Optical microcavities. Nature **424**, 839–846 (2003)
3. L. He, A.K. Zdemir, J. Zhu, W. kim, L. Yang, Detecting single viruses and nanoparticles using whispering gallery microlasers. Nat. Nanotechnol. **6**, 428–432 (2011)
4. M.R. Lee, P.M. Fauchet, Two-dimensional silicon photonic crystal based biosensing platform for protein detection. Opt. Express **15**, 4530–4535 (2007)
5. Q. Li, Z. Li, N. Li, X. Chen, P. Chen, X. Shen, W. Lu, High-polarization-discriminating infrared detection using a single quantum well sandwiched in plasmonic micro-cavity. Sci. Rep. **4**, 6332 (2014)
6. Z. Li, J.-L. Kou, M. Kim, J.O. Lee, H. Choo, Highly efficient and tailorable on-chip metal-insulator-metal plasmonic nanofocusing cavity. ACS Photonics **1**, 944–953 (2014)
7. S. Cui, X. Zhang, T.-L. Liu, J. Lee, D. Bracher, K. Ohno, D. Awschalom, E.L. Hu, Hybrid plasmonic photonic crystal cavity for enhancing emission from near-surface nitrogen vacancy centers in diamond. ACS Photonics **2**, 465–469 (2015)
8. X. Wang, B. Palpant, Large and ultrafast optical response of a one-dimensional plasmonic-photonic cavity. Plasmonics **8**, 1647–1653 (2013)
9. R.F. Oulton, V.J. Sorger, T. Zentgraf, R.-M. Ma, C. Gladden, L. Dai, G. Bartal, X. Zhang, Plasmon lasers at deep subwavelength scale. Nature **461**, 629–632 (2009)
10. S.-W. Chang, C.-Y. Lu, S.L. Chuang, T.D. Germann, U.W. Pohl, D. Bimberg, Theory of metal-cavity surface-emitting microlasers and comparison with experiment. IEEE J. Sel. Top. Quantum Electron **17**, 1681–1692 (2011)
11. C.-Y. Lu, S.-W. Chang, S.L. Chuang, T.D. Germann, D. Bimberg, Metal-cavity surface-emitting microlaser at room temperature. Appl. Phys. Lett. **96**, 251101 (2010)
12. A.M. Lakhani, M.-K. Kim, E.K. Lau, M.C. Wu, Plasmonic crystal defect nanolaser. Opt. Express **19**, 18237–18245 (2011)
13. T.-L. Liu, K.J. Russell, S. Cui, E.L. Hu, Two-dimensional hybrid photonic/plasmonic crystal cavities. Opt. Express **22**, 8219–8225 (2014)
14. Y.-J. Lu, C.-Y. Wang, J. Kim, H.-Y. Chen, M.-Y. Lu, Y.-C. Chen, W.-H. Chang, L.-J. Chen, M.I. Stockman, C.-K. Shih, S. Gwo, All-color plasmonic nanolasers with ultralow thresholds: autotuning

15. M.J.H. Marell, B. Smalbrugge, E.J. Geluk, P.J.V. Veldhoven, B. Barcones, B. Koopmans, R. Nötzel, M.K. Smit, M.T. Hill, Plasmonic distributed feedback lasers at telecommunications wavelengths. Opt. Express **19**, 15109–15118 (2011)
16. M.A. Noginov, G. Zhu, A.M. Belgrave, R. Bakker, V.M. Shalaev, E.E. Narimanov, S. Stout, E. Herz, T. Suteewong, U. Wiesner, Demonstration of a spaser-based nanolaser. Nature **21**, 1110–1112 (2009)
17. R.F. Oulton, Surface plasmon lasers: sources of nanoscopic light. Mater. Today **15**, 26–34 (2012)
18. X. Zhu, J. Zhang, J. Xu, D. Yu, Vertical plasmonic resonant nanocavities. Nano Lett. **11**, 1117–1121 (2011)
19. Y.-H. Chou, Y.-M. Wu, K.-B. Hong, B.-T. Chou, J.-H. Shih, Y.-C. Chung, P.-Y. Chen, T.-R. Lin, C.-C. Lin, S.-D. Lin, T.-C. Lu, High-operation-temperature plasmonic nanolasers on single-crystalline aluminum. Nano Lett. **16**, 3179–3186 (2016)
20. H. Jiang, C. Liu, P. Wang, D. Zhang, Y. Lu, H. Ming, High-Q/V_{eff} gap-mode plasmonic FP nanocavity. Opt. Express **21**, 4752–4757 (2013)
21. P.-J. Cheng, C.-Y. Weng, S.-W. Chang, T.-R. Lin, C.-H. Tien, Plasmonic gap-mode nanocavities with metallic mirrors in high-index cladding. Opt Express **21**, 13479–13491 (2013)
22. Y.-H. Chou, B.-T. Chou, C.-K. Chiang, Y.-Y. Lai, C.-T. Yang, H. Li, T.-R. Lin, C.-C. Lin, H.-C. Kuo, S.-C. Wang, T.-C. Lu, Ultrastrong mode confinement in ZnO surface plasmon nanolasers. ACS Nano **9**, 3978–3983 (2015)
23. Y.-C. Chung, P.-J. Cheng, Y.-H. Chou, B.-T. Chou, K.-B. Hong, J.-H. Shih, S.-D. Lin, T.-C. Lu, T.-R. Lin, Surface roughness effects on aluminium-based ultraviolet plasmonic nanolasers. Sci. Rep. **7**, 39813 (2017)
24. X. Yang, A. Ishikawa, X. Yin, X. Zhang, Hybrid photonic-plasmonic crystal nanocavities. ACS Nano **5**, 2831–2838 (2011)
25. J.D. Joannopoulos, S.G. Johnson, J.N. Winn, R.D. Meade, *Photonic crystals: molding the flow of light*. (Princeton university press, Princeton, 2011)
26. T.-R. Lin, S.-W. Chang, S.L. Chuang, Z. Zhang, P.J. Schuck, Coating effect on optical resonance of plasmonic nanobowtie antenna. Appl. Phys. Lett. **97**, 063106 (2010)
27. S.Y. Lee, L. Hung, G.S. Lang, J.E. Cornett, I.D. Mayergoyz, O. Rabin, Dispersion in the SERS enhancement with silver nanocube dimers. ACS Nano **4**, 5763–5772 (2010)
28. C. Sun, K.-H. Su, J. Valentine, Y.T. Rosa-Bauza, J.A. Ellman, O. Elboudwarej, B. Mukherjee, C.S. Craik, M.A. Shuman, F.F. Chen, X. Zhang, Time-resolved single-step protease activity quantification using nanoplasmonic resonator sensors. ACS Nano **4**, 978–984 (2010)
29. J. McPhillips, A. Murphy, M.P. Jonsson, W.R. Hendren, R. Atkinson, F. Hook, A.V. Zayats, R.J. Pollard, High-performance biosensing using arrays of plasmonic nanotubes. ACS Nano **4**, 2210–2216 (2010)
30. K. Hakuta, K.P. Nayak, Manipulating single atoms and photons using optical nanofibers. Adv. Nat. Sci. Nanosci. Nanotechnol. **3**, 015005 (2012)
31. J.D. Christesen, C.W. Pinion, E.M. Grumstrup, J.M. Papanikolas, J.F. Cahoon, Synthetically encoding 10 nm morphology in silicon nanowires. Nano Lett. **13**, 6281–6286 (2013)
32. F. Vollmer, L. Yang, Review label-free detection with high-Q microcavities: a review of biosensing mechanisms for integrated devices. Nanophotonics **1**, 267–291 (2012)
33. D. Benelarbi, T. Bouchemat, M. Bouchemat, Design of high-sensitive refractive index sensor using a ring-shaped photonic crystal waveguide. Nanosci. Nanotechnol. **6**(1A), 105–109 (2016)
34. B. Wawng, G.P. Wang, Plasmon bragg reflectors and nanocavities on flat metallic surfaces. Appl. Phys. Lett. **87**, 013107 (2005)